Phase-sensitive optical detection of ballistic phonon heat pulses using frequency-modulation spectroscopy and persistent spectral holes

W. P. Ambrose and W. E. Moerner
IBM Research Division, Almaden Research Center, San Jose, California 95120
(Received 21 May 1990)

With the use of laser frequency-modulation (FM) spectroscopy and persistent spectral holes, time-resolved phase-sensitive probing of ballistic phonon heat pulses is accomplished in the interior of a NaF crystal. The ballistic phonon heat pulses are generated by the absorption of a Nd:YAG (neodymium-doped yttrium aluminum garnet) laser pulse in a Cr film on the sample surface. Local measurement of the propagating stress-strain field is illustrated by detecting the modulation of a spectral hole in the inhomogeneously broadened 607-nm color-center absorption in x-irradiated NaF at liquid-helium temperatures. By examining the dependence of the observed phonon time-of-flight data on the polarization of the probing light, the position within the sample, and the phase of FM detection, an identification of the acoustic polarizations of the propagating phonons may be made. The effects of phonon focusing and mode conversion upon reflection must be taken into account to complete the identification. Along with the ability to determine the sign of the acoustic disturbance, this experiment features a strain detection limit of 4×10^{-9} at a time resolution of 50 ns.

I. INTRODUCTION

The study of the propagation of nonequilibrium phonons in solids has provided fertile ground for the observation of several novel physical effects.[1] Using heat-pulse generation in constantan films and detection with superconducting bolometers,[2,3] a fascinating phonon-focusing effect was identified due to the intrinsic elastic anisotropy in cubic crystals.[4,5] Phonon focusing has led to the development of a variety of powerful techniques for imaging laser-generated phonon pulses,[6,7] including the study of phonon storage effects in the "hot spot" near the generation region.[8,9]

In contrast to surface detection with ultrasonic transducers and superconducting bolometers, several optical methods for the study of phonons have appeared which allow probing of phonon dynamics and propagation within the bulk of a solid material. In an early experiment,[10] the R-line fluorescence of Cr^{3+} ions in ruby was used as a monitor of 29 cm^{-1} phonons. This experiment and others allowing the detection of high-frequency phonons by phonon-induced fluorescence have been reviewed recently.[11] In recent experiments, enhanced optical dephasing, as measured by optical free-induction decay[12] and modulation of two-pulse photon-echo decays,[13] have both been shown to be sensitive detectors of high- and low-frequency phonons.

Persistent spectral holes also provide a sensitive optical detector of phonon wave packets.[14] In persistent spectral hole burning, the profile of an inhomogeneously broadened optical absorption of a defect in a solid at low temperatures is modified by direct photochemistry or by photophysical modification of the local environment of the absorbing defect.[15] The narrow spectral width of the resulting persistent spectral hole (PSH) allows interaction with acoustic waves with quite high sensitivity. In the first experiment of this type,[14] an ultrasonically generated phonon pulse was shown to lead to strong (phase-insensitive) modulation of a spectral hole with a 5-μs time resolution. By careful control of an impressed ultrasonic field, the resulting shifting and splitting of a spectral hole was shown to lead to both phase-insensitive[16] and phase-sensitive[17] detection techniques for spectral holes themselves. In recent studies, phonon-induced changes of a spectral hole and anti-Stokes phonon sideband methods have been used to study heat-pulse propagation in thin polymer films.[18]

In this paper, the powerful method of laser frequency-modulation spectroscopy (FMS) is used to time-resolve the changes in a persistent spectral hole with a 50-ns time resolution caused by the passage of laser-generated acoustic phonon wave packets through the detection region. In FMS,[19] a frequency-modulated laser beam is converted to an amplitude-modulated beam by the narrow absorption and dispersion due to the spectral hole. The choice of absorption or dispersion line shape and probe laser detuning from the spectral hole determine the sensitivity of the technique and the range of phonon wavelengths, which are detected in the following manner. In one mode of detection, any splitting pattern of the persistent spectral hole that is produced by phonon strains is detected by measuring changes in the absorption hole depth. In principle, by measuring changes in the hole depth, phonons of any wavelength and frequency may be detected. However, since the hole depth decreases for any splitting pattern, changes in the hole depth do not contain information about the phase of the phonons.

A more sensitive mode of detection is obtained by detecting net shifts or asymmetric splitting at the zero crossing or high-slope region of a dispersion line shape. In this case, the wavelength of detected phonons must be larger than the probe beam diameter, since a net asym-

metric splitting of the hole is required to produce a signal. (Phonons with wavelengths smaller than the probe beam diameter produce a net symmetric splitting over the probe volume.) The sign of the signal indicates the sign of the net frequency shift of the hole, which does contain information about the phase or sign of the phonon strain field. In this phase-sensitive mode of detection, the detected phonons are in the 0–20 MHz frequency range, which is at the low-frequency (ultrasonic) end of the acoustic phonon dispersion curve. Since the detection operates at a high rf frequency far above the laser low-frequency noise spectrum, the technique can operate near the shot-noise limit.

To illustrate the technique, the 607-nm zero-phonon optical absorption of aggregate color centers in NaF was chosen as the inhomogeneously broadened optical transition capable of PSH formation. Time-of-flight data for phonon wave packets generated by the absorption of neodymium-doped yttrium aluminum garnet (Nd:YAG) laser pulses in a metal film in this system have a rich structure, requiring a fairly detailed analysis. In Sec. II, the experimental methods used to record laser-generated phonon time-of-flight signals are described. In Sec. III, the theory of phonon-induced splitting and shifting of the optical transition is developed. In Sec. IV, experimental results on phonon detection and probe polarization dependence are presented. The technique is demonstrated to be sensitive to strains of 4×10^{-9}. In Sec. V, the dependence of the time-of-flight data on laser position along with the theory of Sec. III are utilized to identify the acoustic polarizations of the various phonon peaks. Since this technique is able to measure the stress and strain of ballistic phonon peaks in the interior of a solid with high time resolution, it should prove to be useful for the study of phonon dynamics and propagation in a variety of materials.

II. EXPERIMENT

Figure 1 shows the sample configuration for laser generation and phase-sensitive time-of-flight detection of phonons. The material studied in these experiments is single-crystal NaF containing aggregate color centers. Ballistic packets of acoustic phonons are generated by Nd:YAG laser pulses incident on a thin film of Cr that has been evaporated on one face of the NaF crystal. Phonons propagating away from the Cr film into the NaF crystal are detected inside a selected crystal volume by a probe-laser beam. The basic physical phenomenon used in the detection process is that phonon stress and strain fields shift and split the color-center absorption lines. For sensitive detection of the absorption frequency shifts, the probe laser is first used to burn a narrow PSH in the inhomogeneously broadened 607-nm color-center zero-phonon line (ZPL).[20–22] The phonons are then detected as small frequency shifts of the PSH using wide-bandwidth laser FMS.[19] Notice that both the phonon-generation and probe-laser beams may be displaced to examine the propagation behavior of phonons inside the crystal. The Cartesian coordinate system shown in Fig. 1, with origin centered on the Cr-coated end face and axes along ⟨100⟩ cubic-crystal directions, will be used throughout this paper to describe the positions of the laser beams and the components of the phonon stress tensor.

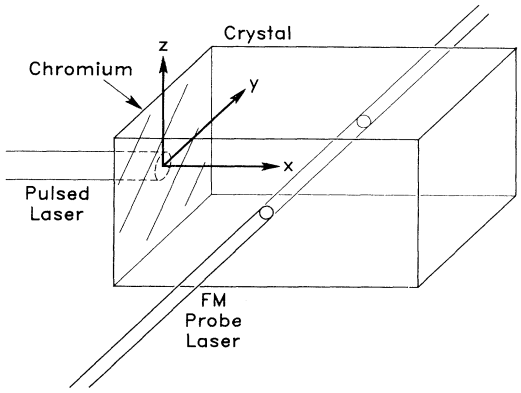

FIG. 1. Sample configuration for laser generation and phase-sensitive time-of-flight detection of phonons. A thin film of Cr is evaporated on one face of a single crystal of NaF. The crystal contains color centers, has polished {100} faces, and is immersed in superfluid He at 1.6 K. A pulsed Nd:YAG laser beam is used to generate heat pulses in the Cr film. A probe-laser beam is used to burn a narrow persistent spectral hole in a color-center zero-phonon line. Subsequent frequency modulation of the probe-laser beam allows broadband detection of the modulation of the hole shape by the phonon pulses.

The sample consisted of a single crystal of NaF, cleaved and polished along {100} crystal planes with dimensions of $1\times1\times2$ cm^3. Color centers were produced by exposing one of the 1×1-cm^2 crystal faces to Cu x rays (30 mA at 30 kV) for 305 h at room temperature. The crystal acquired a gradient of pinkish brown color from the irradiated end. A 0.3-μm layer of Cr was evaporated on the face opposite the irradiated face. For convenience, the NaF color-center aggregate with ZPL at 607 nm was chosen as the inhomogeneously broadened optical transition capable of PSH formation.[20] The 607-nm ZPL had an internal transmittance of 90% through 1 cm near the middle of the crystal at 1.6 K, as measured with a tungsten lamp, a $\frac{3}{4}$-m monochromator, and a GaAs photomultiplier tube.

Figure 2 shows the experimental apparatus for phase-sensitive time-of-flight detection of ballistic phonon packets. The subsystems of the apparatus are a frequency-modulated cw dye laser probe beam, a pulsed Nd:YAG laser beam used to generate phonons in the sample held at 1.6 K in an optical immersion cryostat, and high-speed laser-frequency-modulation detection electronics. Details for each of these subsystems will be presented first, followed by a brief elaboration for certain components and the procedure used to obtain phonon time-of-flight signals.

A single-frequency R6G dye laser (DL) (Coherent 599-21) beam, with a jitter-limited linewidth of 3 MHz, passes through a Faraday optical isolator (OI), an amplitude stabilizer (AS), and a $LiTaO_3$ electro-optic phase modulator (EOM) (Crystal Technology Model 6100) driven at 250

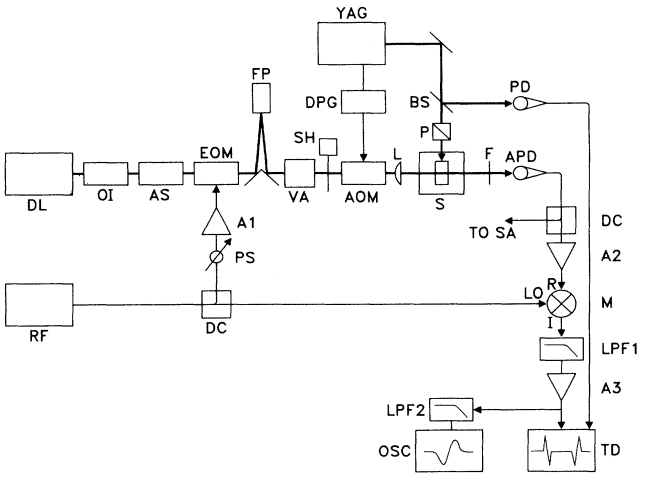

FIG. 2. Experimental apparatus for phase-sensitive time-of-flight detection of phonons. The subsystems of the apparatus are a frequency-modulated dye laser probe beam (DL), a pulsed Nd:YAG laser beam (YAG) used to generate phonons in a sample (S) held at 1.6 K in an optical immersion cryostat, and standard high-speed laser FM detection electronics. A detailed description of the apparatus is given in the text.

MHz. The phase modulator produces a frequency-modulated laser beam which is reflected from a confocal Fabry-Pérot etalon (FP) with a 7.5-GHz free spectral range, is attenuated with fixed and variable attenuators (VA), and can be blocked with a mechanical shutter (SH) while performing diagnostics with the FP. Opening the shutter allows the dye laser beam to pass through a high-speed acousto-optic modulator shutter (AOM) (Isomet 1205-603D) and to be focused into the sample (S) with a lens (L). The transmitted probe beam is detected with a high-speed Si avalanche photodiode (APD) (Analog Modules LNCA, 275 MHz bandwidth, and -210 V bias). The laser beam diameter varies from 75 to 100 μm in the sample.

A Q-switched Nd:YAG laser (YAG) is operated at 1.06 μm and produces 8-ns-long pulses at a repetition rate of 6 Hz. The YAG laser beam is split with a glass beam splitter (BS) to produce detection-triggering and phonon-generation beams. The reflected YAG laser beam is converted to an electronic trigger by a 300-MHz bandwidth Si p-i-n photodiode (PD). The transmitted beam is expanded and apertured to 0.1 cm for uniform illumination, and is attenuated to 1–10 μJ/pulse with a polarizer (P) before hitting the sample. Since the APD can also detect YAG laser scattered light, any scattered YAG radiation is blocked with several short pass interference filters (F).

The AOM in the probe beam is used as a fast shutter to expose the sample to the probing light for only a short time about the YAG firing time (the reason for this is explained below). The AOM needs to be turned on some time before the YAG laser fires. Since the YAG laser lamps fire before the YAG reaches threshold, the lamp signal is used to trigger a digital delay generator (DPG), the output of which is used to open the AOM. Jitter in the lamp-to-laser firing time is unimportant, since the transient digitizer is triggered by the laser pulse itself.

Standard laser FMS techniques are used to sensitively detect the time variation of a persistent spectral hole in a 20-MHz bandwidth.[19,23] The sensitivity results from detection at a frequency above the laser excess noise spectrum, where the laser noise is mostly shot noise. An rf source, operating at $\nu_{rf}=250$ MHz and $+7$ dB m, is split with a -10-dB directional coupler (DC), the split signal of which is phase shifted (PS), amplified (A1) ($+32$ dB), and used to drive the EOM. The through port of the DC drives the local oscillator (LO) port of the rf mixer (M) (minicircuits ZFM-3). As is usual in FMS, the frequency spectrum at the output of the EOM consists of a carrier (the dye laser frequency) and two sidebands spaced above and below the carrier by $\pm\nu_{rf}$ with one sideband in phase with the carrier and the other sideband 180° out of phase with the carrier. When heterodyne mixing of the sidebands with the carrier occurs in the APD, a 180° phase difference results between the two beat signals at ν_{rf}. With the sidebands balanced, the beat signals cancel, and there is no rf photocurrent from the APD at ν_{rf}. If a sharp spectral feature such as a persistent spectral hole with width on the order of ν_{rf} is probed by the sidebands, the resulting imbalance in the sidebands is translated into a photocurrent in the APD at ν_{rf}. The detected rf signal is amplified by A2 ($+34$-dB gain, 2–500 MHz) and sent to the rf (R) port of the mixer. At the IF (I) port of the mixer, a 20-MHz low pass filter (LPF1) blocks sum frequencies, and passes the envelope of the rf signal which emerges from the APD in a 20-MHz bandwidth about ν_{rf}. The (time-dependent) envelope signal is further amplified in A3 (gain of 20, 0–150 MHz) and sent to either (1) a transient digitizer (TD) to record the phonon time-of-flight signals with the laser frequency held fixed, or (2) a 2-kHz low pass filter (LPF2) and an oscilloscope (OSC) to obtain a FM spectrum of the hole shape by tuning the laser frequency about the hole.

Before phonon time-of-flight spectra are obtained, a PSH is burned in the sample absorption spectrum. The probe laser is tuned to the red of the 607-nm ZPL, the positions of the laser beams are selected in the sample, and the crystal is oriented normal to the probe beam. The probe-laser polarization is selected with a Fresnel rhomb, and the laser is tuned to a position near the center of the ZPL at a wavelength between 607.145 and 607.135 nm. The laser vacuum wavelength is measured with a wave meter. A PSH is then burned into the ZPL spectrum with the dye laser frequency fixed, FM off, and the AOM on. The hole-burning time is typically 5–7 min using 200 μW in a beam diameter of 75 μm.

After a hole is burned, the PSH FM spectrum is displayed on the OSC in order to adjust the rf phase and select a laser frequency for phonon detection. The adjustment process requires about a minute, and so the probe-laser intensity is reduced to 2 μW to reduce subsequent hole burning during the setup process. At this power level, the 2-kHz low pass filter bandwidth of LPF2 is adequate for recording the PSH FM spectrum with a signal-to-noise ratio (SNR) of about 10 in one 0.25-s scan.

Figure 3 shows PSH shapes in the NaF 607-nm ZPL at 1.6 K as measured with FMS by scanning the dye laser. Figure 3(a) is the absorptive or S_1 phase (in phase with the rf source) and Fig. 3(b) is the dispersive or S_2 phase (quadrature phase) PSH frequency modulated spectrum.[19,23] The S_1-phase spectrum in Fig. 3(a) contains two copies of the absorption hole shape, each produced as an FM sideband is tuned through the PSH. Modeling the FM line shape reveals that these holes have hole widths [full width at half maximum (FWHM)] on the order of modulation frequency of 250 MHz. This hole width is somewhat larger than the true low-intensity width of 45±6 MHz (Ref. 20) due to the need to use a relatively tight focus in the sample. The S_2-phase spectrum is composed of three overlapping copies of the PSH dispersion, one centered at the hole-burning frequency, and two others displaced by $\pm\nu_{rf}$ with half the amplitude of the central feature. The depth of the absorption hole producing the FM line shapes in Fig. 3 is calibrated using the size of the reflection dip of the etalon and the etalon FM spectrum. Holes burned near the middle of the sample typically consist of about a 5% change in transmission.

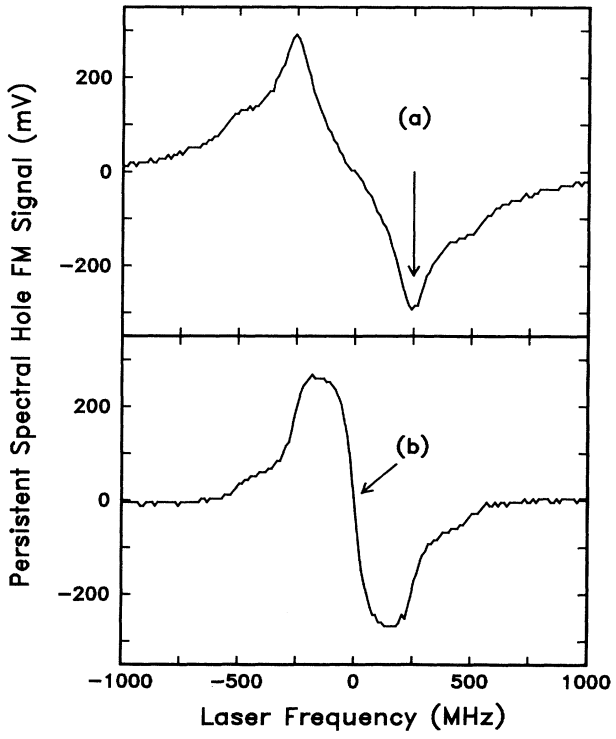

FIG. 3. Persistent spectral hole frequency-modulation spectra. A persistent spectral hole (PSH) is burned into the NaF 607-nm color-center zero-phonon line at 1.6 K while the laser frequency modulation is off. FM spectra of the PSH are measured by tuning the laser frequency through 2 GHz about the burn frequency while the laser frequency is modulated at 250 MHz. The FM spectra are shown in (a) S_1 or absorption phase and (b) S_2 or dispersion phase. The arrows point to the frequencies at which the laser is fixed in order to detect the modulation of the hole shape by phonons.

To obtain phonon time-of-flight signals, the rf phase of detection is selected to be either S_1 or S_2, the etalon signals are tuned away from the PSH, and the laser frequency is fixed. In S_2 phase, the laser frequency is fixed at the high-slope region at the center of the hole spectrum [Fig. 3(b)]. In S_1 phase, the laser frequency is fixed at the negative peak of the negative copy of the absorption hole [Fig. 3(a)]. With no modulation of the hole shape, the output of the mixer remains constant at zero (for S_2) or at the negative peak value (for S_1). When phonon pulses propagate through the hole-burned volume, the PSH splits under the influence of phonon stress and strain, and the hole modulation signals are recorded and averaged on the TD.

As is well known for spectral holes in color-center ZPL's (Ref. 24), excessive reading intensity can cause distortion of the PSH shape by additional hole burning. At the same time, since the fast phonon time-of-flight signals are recorded with a 20-MHz detection bandwidth, higher reading powers are required to maintain SNR compared to the case with a 2-kHz bandwidth. To satisfy these conflicting requirements, the AOM is used as a shutter to transmit the 20-μW dye laser beam to the sample only during the phonon time-of-flight detection period. This reduces the duty cycle to (100 μs) (6 Hz)=0.0006, where 100 μs is the longest recording interval used. Each time-of-flight signal is typically averaged over 1500 YAG laser shots, for a signal integration time less than 0.15 s per averaged trace, but the total experiment time is nearly 4 min. In this manner, a higher phonon time-of-flight SNR is achieved with lower total probe-laser flux and insignificant additional hole burning.

III. DETECTION THEORY

Phonon propagation experiments frequently employ pulsed laser heating of a metal surface to generate phonon pulses.[25–27] In the nonablative, low-power or thermoelastic regime, the laser radiation is absorbed within a few hundred Å of the metal surface. The microscopic view at low temperatures is that the absorbed laser energy quickly converts to lattice vibrations or phonons with a uniform distribution of phase velocity directions. For the YAG pulse fluences used in these experiments, the surface temperature is estimated to be higher than 15 K, which results in a distribution of phonon frequencies up to approximately 0.5 THz. This frequency is well below the optic phonon spectrum and in the range of acoustic phonons for NaF. The laser-pulse-generated acoustic phonons propagate into the crystal in three separate expanding shells or wave packets, one composed of longitudinal and the other two composed of transverse acoustic phonons.[26,28] Since the phonons contributing to the ballistic phonon pulses that we observe are of fairly low frequency and in the linear dispersion region, we may in a reasonable approximation focus on only one type of low-frequency phonon at a time. This is a result of the fact that all the phonons of interest in a particular polarization propagating in a fixed direction have the same velocity characteristics. The resulting total signal will be a superposition of the physical effects from all the phonons

present.

The basic idea behind detecting a phonon with a persistent spectral hole is that the phonon is a traveling stress-strain field and that the spectral hole splits and shifts under the influence of stress and strain. The ability of the probe-laser beam to phase-sensitively detect the perturbations due to the local stress-strain field depends upon the detection bandwidth as well as the relative size of the probe beam diameter and the phonon wavelength. In these experiments, the probe beam diameter is smaller than one-half the minimum acoustic wavelength expected for 20-MHz phonons in NaF; therefore, the ability to follow the time dependence (and sign) of phonons up to the bandwidth limit of 20 MHz is expected.

In the standard anisotropic continuum limit, a wave equation for the displacement of volume elements in the solid has plane-wave solutions of the form[29,30]

$$\mathbf{u}(\mathbf{r},t)=\mathbf{u}_0\exp[i(\mathbf{k}\cdot\mathbf{r}-\omega t)] , \tag{1}$$

where $\mathbf{u}_0$ is the polarization of the acoustic wave, $\mathbf{k}$ is its wave vector, and ω is its frequency. There are three different phase velocity surfaces $\mathbf{v}_p=(\omega/k)\hat{\mathbf{k}}$ in $\mathbf{k}$ space, where $\hat{\mathbf{k}}$ is a unit vector in the direction of $\mathbf{k}$. The three surfaces correspond to different orthogonal displacement polarizations. The phase velocity surface with polarization $\mathbf{u}_0$ nearly parallel to $\mathbf{v}_p$ is known as the quasilongitudinal surface, and the other two are the quasishear or quasitransverse surfaces. The strain tensor for the displacement wave in Eq. (1) is formed from the symmetric part of the gradient tensor[31,32] and has (real) components

$$\epsilon_{ij}=-\tfrac{1}{2}(u_i k_j+u_j k_i)\sin(\mathbf{k}\cdot\mathbf{r}-\omega t) . \tag{2}$$

Equivalently, the stress in the wave may be computed through the elastic stiffness tensor as

$$\sigma_{ij}=C_{ijkl}\epsilon_{kl} , \tag{3}$$

where summation over repeated indices is assumed. It is useful to work with the stress tensor since a connection can directly be made to previous uniaxial stress calculations[33] and experiments[34] for the 607-nm NaF color center.

Following Kaplyanskii,[33] the absorption frequency shift for a single defect under externally applied stress may be written in a linear approximation as

$$\Delta=A_{xx}\sigma_{xx}+A_{yy}\sigma_{yy}+A_{zz}\sigma_{zz}+2A_{xy}\sigma_{xy}+2A_{yz}\sigma_{yz}+2A_{zx}\sigma_{zx} , \tag{4}$$

where the A_{ij} are the components of the piezospectroscopic tensor for the defect. The piezospectroscopic tensor components depend on the symmetry allowed possible defect orientations in the crystal.

The symmetry of the 607-nm NaF color center used in this work was previously examined with polarized spectroscopy of the entire ZPL under uniaxial stress[34] and pseudo-Stark splitting of PSH's under dc electric fields.[21] The 607-nm NaF color center has C_s symmetry, and its ZPL transition moment $\boldsymbol{\mu}$ is perpendicular to the $\{110\}$ oriented defect reflection planes.[21] Defects with C_s symmetry in a cubic lattice are referred to as monoclinic type I defects, for which there are 12 equivalent but distinct orientations of the $\{110\}$ oriented defect planes.[33] The presence of a reflection plane of symmetry limits the number of independent A_{ij} to four, which are labeled A_i, with $i=1$, 2, 3, and 4. Table I presents the energy shift coefficients in Eq. (4) for each of the 12 defect orientations. By examing Table I and Eq. (4), one can see that each defect orientation has a different absorption frequency shift for an arbitrary stress. With no applied stress or strain, defects with the same transition energy are orientationally degenerate. The PSH splitting results when phonon stress lifts the orientational degeneracy.

To use these frequency shifts as a detector of stress or strain, we must also know the amount that each of the possible defect orientations contributes to a PSH, i.e., we need the size of the components in the splitting pattern. These are not the same size as the components in a linear absorption splitting pattern. Defects with transition moments in a direction $\boldsymbol{\mu}_i$ are hole burned at a rate proportional to $|\boldsymbol{\mu}_i\cdot\mathbf{p}|^2$, where $\mathbf{p}$ is the laser polarization. For shallow holes, the contribution to the hole depth is proportional to the product of the rate at which defects of a particular orientation are hole burned and their unburned absorption strength, i.e., defects with $\boldsymbol{\mu}_i$ contribute an

TABLE I. Persistent-spectral-hole stress-shift coefficients for monoclinic (type-I) defects in cubic crystals.

			Coefficient for stress component					
i	$\hat{\boldsymbol{\mu}}_i$	f_i	σ_{xx}	σ_{yy}	σ_{zz}	σ_{xy}	σ_{yz}	σ_{zx}
1	110	α^4	A_2	A_2	A_1	$2A_3$	$2A_4$	$-2A_4$
2	$\bar{1}\,\bar{1}0$	α^4	A_2	A_2	A_1	$2A_3$	$-2A_4$	$2A_4$
3	$1\bar{1}0$	α^4	A_2	A_2	A_1	$-2A_3$	$-2A_4$	$-2A_4$
4	$\bar{1}10$	α^4	A_2	A_2	A_1	$-2A_3$	$2A_4$	$2A_4$
5	101	$\lvert\alpha+\gamma\rvert^4$	A_2	A_1	A_2	$-2A_4$	$-2A_4$	$-2A_3$
6	$\bar{1}0\bar{1}$	$\lvert\alpha+\gamma\rvert^4$	A_2	A_1	A_2	$2A_4$	$2A_4$	$-2A_3$
7	$10\bar{1}$	$\lvert\alpha-\gamma\rvert^4$	A_2	A_1	A_2	$2A_4$	$-2A_4$	$2A_3$
8	$\bar{1}01$	$\lvert\alpha-\gamma\rvert^4$	A_2	A_1	A_2	$-2A_4$	$2A_4$	$2A_3$
9	$01\bar{1}$	γ^4	A_1	A_2	A_2	$-2A_4$	$2A_3$	$2A_4$
10	$0\bar{1}1$	γ^4	A_1	A_2	A_2	$2A_4$	$2A_3$	$-2A_4$
11	011	γ^4	A_1	A_2	A_2	$2A_4$	$-2A_3$	$2A_4$
12	$0\bar{1}\,\bar{1}$	γ^4	A_1	A_2	A_2	$-2A_4$	$-2A_3$	$-2A_4$

amount $f_i = |\mu_i \cdot \mathbf{p}|^4$ to the hole depth. In the experiment, the laser is linearly polarized in the x-z plane (see Fig. 1) with direction cosines α and γ from the x and z directions. Table I also shows the unnormalized contribution f_i that each defect orientation provides to the hole depth in terms of the laser polarization direction cosines. With the values in Table I, any splitting pattern may be computed for a persistent spectral hole burned in the NaF 607-nm color-center ZPL for an arbitrary stress and laser polarization in the x-z plane.

Before using the complete hole-splitting pattern to calculate the phonon signals, we consider the signal that results from a net frequency shift of the entire hole. A shift of the entire hole displaces the FM spectra in Fig. 3 along the frequency axis. The highest sensitivity is obtained at the center of the dispersion-like S_2 signal in Fig. 3(b), since this is the position of highest slope in the PSH FM spectra. Note that the sign of the signal indicates the sign of the net frequency shift of the hole. On the other hand, when the stress produces a symmetric splitting of the hole, no large signal results for laser frequency fixed at the center of the S_2 spectrum. Hence, it is also useful to detect the effects of stress for another laser frequency and rf phase, as shown in Fig. 3(a). With the laser frequency fixed at the S_1 negative peak in Fig. 3(a), any splitting pattern of the hole, symmetric or asymmetric, decreases the hole depth which is detected as an increase in signal. The sign of the signal in S_1 phase is always positive regardless of the type of splitting. In other words, the center of S_2 is used to phase-sensitively detect net frequency shifts due to asymmetric splitting, and the peak of S_1 is used to detect any splitting.

The S_2 signal for the three probe-laser polarizations used in the experiment may now be computed. The dispersion for a Lorentzian-shaped hole may be written[23] as

$$\phi(\nu)=\delta_p \left[\frac{\nu(\Gamma/2)}{\nu^2+(\Gamma/2)^2} \right] , \tag{5}$$

where δ_p is a magnitude factor, Γ is the full width at half maximum of the absorption hole, and the hole is centered at zero frequency. The S_2 spectrum is proportional to[19,23]

$$S_2(\nu) \sim \phi(\nu-\nu_{\rm rf})+\phi(\nu+\nu_{\rm rf})-2\phi(\nu) . \tag{6}$$

The approximation assumed in Eq. (6) is the limit of small modulation index and shallow holes. A modulation index near 1 is used in these experiments, for which higher-order terms in $\nu_{\rm rf}$ should be important in the entire spectrum $S_2(\nu)$. However, we will only be concerned with the slope of the $S_2(\nu)$ spectrum near the center of the PSH and thus can negelect these higher-order terms with large spacing from the center of the hole. For a small shift of the entire hole by Δ, a linear approximation to the S_2 phase signal with laser frequency fixed at the burn frequency is

$$S_2(\Delta) \sim -\delta_p \frac{4}{\Gamma} \left[1+ \left[\frac{\Gamma/2}{\nu_{\rm rf}} \right]^2 \right]^{-1} \Delta \equiv F(\nu_{\rm rf},\Gamma,\delta_p)\frac{\Delta}{\Gamma} , \tag{7}$$

where $F(\nu_{\rm rf},\Gamma,\delta_p)$ is constant for fixed $\nu_{\rm rf}$, Γ, and δ_p. Equation (7) reasonably predicts that the slope of the S_2 spectrum increases with the hole size δ_p, increases with the FM sideband spacing $\nu_{\rm rf}$, and decreases with the hole width Γ. When the orientational degeneracy of the hole is lifted by stress, the S_2 signal is proportional to

$$S_2 \sim \frac{\sum_i f_i S_2(\Delta_i)}{\sum_i f_i} = \frac{F}{\Gamma} \frac{\sum_i f_i \Delta_i}{\sum_i f_i} , \tag{8}$$

where the component sizes f_i and the shifts Δ_i are computed from the information in Table I. Note that through Table I, Eq. (8) is linear in the small stress or strain tensor components of a phonon [Eq. (8) may be written in terms of the strain using Eq. (3)].

In the experiments presented in subsequent sections, three different probe-laser polarizations were examined: (1) $+45°$ ($\alpha=\gamma=1/\sqrt{2}$), (2) $-45°$ ($\alpha=-\gamma=1/\sqrt{2}$), and (3) horizontal or $0°$ ($\alpha=1,\gamma=0$). The S_2 signals for these three laser polarizations are computed from Eq. (8) and Table I to be

$$S_2^{+45} \sim \frac{F}{\Gamma} \tfrac{1}{10}[(A_1+9A_2)\sigma_{xx}+(8A_1+2A_2)\sigma_{yy} +(A_1+9A_2)\sigma_{zz}-16A_3\sigma_{zx}] , \tag{9a}$$

$$S_2^{-45} \sim \frac{F}{\Gamma} \tfrac{1}{10}[(A_1+9A_2)\sigma_{xx}+(8A_1+2A_2)\sigma_{yy} +(A_1+9A_2)\sigma_{zz}+16A_3\sigma_{zx}] , \tag{9b}$$

$$S_2^{0} \sim \frac{F}{\Gamma}[(A_2)\sigma_{xx}+\tfrac{1}{2}(A_1+A_2)\sigma_{yy}+\tfrac{1}{2}(A_1+A_2)\sigma_{zz}] . \tag{9c}$$

The quantities in Eqs. (9) involve one off-diagonal or shear stress component, and linear combinations of the diagonal or axial stress components.

Taking sums and differences of the S_2^{+45} and S_2^{-45} expressions gives

$$\tfrac{1}{2}(S_2^{-45}-S_2^{+45}) \sim \frac{F}{\Gamma} \tfrac{8}{5} A_3 \sigma_{zx} , \tag{10a}$$

$$\tfrac{1}{2}(S_2^{-45}+S_2^{+45}) \sim \frac{F}{\Gamma} \tfrac{1}{10}[(A_1+9A_2)\sigma_{xx} +(8A_1+2A_2)\sigma_{yy} +(A_1+9A_2)\sigma_{zz}] . \tag{10b}$$

Note that taking the sum and difference of the S_2^{+45} and S_2^{-45} signals separates out one off-diagonal shear stress from the diagonal or axial stresses. In other words, through suitable choices of laser polarization and linear combinations of small signals, it is possible to obtain individual stress tensor components for phonons propagating inside a crystal. By converting the measured phonon stress tensor components to strain with Eq. (3), Eq. (2) can then be used to obtain information about the phonon wave vectors and polarizations.

The high symmetry of a cubic crystal simplifies computation of the strains from stress. Cubic symmetry limits

TABLE II. Piezospectroscopic components for NaF 607-nm color centers.

i	A_i kHz/(N/m^2)
1	0.0±0.2
2	2.3±0.8
3	5.4±1.0
4	1.3±0.3

the form of the elastic stiffness tensor in Eq. (3) such that the diagonal stress-strain relations are decoupled from the off-diagonal stress-strain relations.[35] For instance, the off-diagonal stress and strain are simply related by $\epsilon_{ij}=\sigma_{ij}/2C_{44}$, $i\neq j$, and the diagonal stress and strain mix among themselves.

Using Kaplyanskii's uniaxial stress calculations,[33] and Baumann's uniaxial stress data,[34] an estimate for the piezospectroscopic components may be obtained for the NaF 607-nm color center. The A_i are presented in Table II. These coefficients will be useful in gauging the sensitivity of the technique used here in measuring phonon stress and strain.

IV. PHONON DETECTION SENSITIVITY AND PROBE POLARIZATION DEPENDENCE

A. Experimental results

Figure 4 shows the phonon time-of-flight signals for three probe-laser polarizations detected in S_1 and S_2 FM phase, with the probe-laser frequency fixed at the arrows in Fig. 3. The probe laser was positioned at $x=0.94$ cm from the Cr surface, and was vertically centered ($z=0$). The 0.1-cm-diam YAG laser spot was horizontally centered in the Cr face ($y=0$), and displaced to $z=0.05$ cm. (The importance of the YAG spot displacement will become apparent in Sec. V.) The YAG laser firing time is at zero on the time axis in Fig. 4. The S_2-phase signals are at 0 V, and the S_1-phase signals are near -0.75 V. The separation between the S_1 and S_2 signals near $t=0$ is the S_1 FM spectrum negative peak size, and approximately the size of the S_2 FM spectrum peak value. For 1500 averages in a 20-MHz bandwidth, the noise level is about 5% of the peak value of the S_1 or S_2 spectra, which corresponds to a change in transmission of about 0.1%. The signals shown in Fig. 4 clearly represent shifting and splitting of the persistent spectral hole, since no signals are obtained if the same experiments are performed with no persistent spectral hole present.

Signals larger than the noise only appear more than 1.5 μs after the YAG laser fires. The S_1 signals are relatively simple compared to the S_2 signals—each of the S_1 signals contains two large peaks with some structure. The S_1 signals show no qualitative dependence on probe-laser polarization. By comparison, the S_2 signals show much more complicated structure. The largest S_2 signals correspond to the largest S_1 signals, but there are many more S_2 signals above the noise in Fig. 4. Some signals

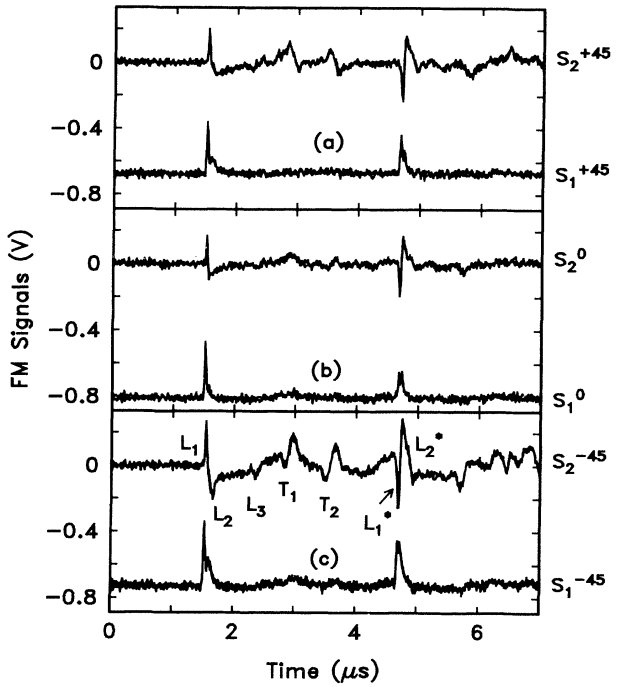

FIG. 4. Phonon time-of-flight signals for three probe-laser polarizations. The probe-laser polarization is fixed at (a) +45° from horizontal, (b) horizontal, or (c) −45° from horizontal. Persistent spectral holes (PSH's) are burned and probed in the same polarization. For a given probe polarization, the time dependence of the PSH is monitored at the negative peak of the S_1-phase FM spectrum or the center of the S_2-phase FM spectrum, as shown in Fig. 3. Each trace is an overlay of two traces, each of which is an average over 1500 Nd:YAG laser shots.

are expected to be smaller in S_1 phase, since the PSH peak size is less sensitive to small frequency shifts than the high slope of S_2 (see Fig. 3). For purposes of later discussion, each of the various signals has been labeled L_1, L_2, L_3, T_1, T_2, L_1^*, and L_2^* in Fig. 4.

The features L_1, L_2, L_1^*, and L_2^*, which show an arrival time correspondence in the S_1 and S_2 signals, can be compared for an understanding of the splitting behavior of the PSH. As described in Sec. III, the S_2 signals only respond to asymmetric splitting (with a net shift) and S_1 records any splitting, however, less sensitively than S_2. The L_1 pulse shows a net upward frequency shift of the hole in any polarization. Comparing the S_1 and S_2 signals as L_1 crosses over into L_2, one observes the PSH to partially recover its unsplit condition, and then split again with a net negative frequency shift. The L_1 pulse is very narrow (20-MHz bandwidth limited), but the L_2 tail following the L_1 pulse lasts for about a microsecond. Note that the L_1^* and L_2^* signals mimic the L_1 and L_2 signals, but with an overall change of sign, and a shorter L_2^* tail.

Unlike the L signals, the T signals show a qualitative dependence on the laser polarization. Note that the T signals in Figs. 4(a) and 4(b) each consist of a frequency

swing of one sign followed by a frequency swing of the opposite sign. This shape shall subsequently be referred to as the "derivative shape" of the T signals. The derivative-shaped features labeled T_1 and T_2 change sign for probe-laser polarization changing from $+45°$ to $-45°$ in Figs. 4(a) and 4(c). Note that the T_1 and T_2 signals are much smaller in Fig. 4(b) for horizontal probe-laser polarization.

One perplexing aspect of the S_2 signal is its richness. A simple view of pulsed phonon propagation is that, for an arbitrary displacement within the solid, one longitudinal and two transverse modes are generated, with the transverse modes propagating with roughly half the longitudinal speed in NaF. The multitude of S_2 arrival times observed cannot all be reconciled with phonons traveling in nearly a $\langle 100 \rangle$ crystal direction. An identification of the phonons giving rise to these signals will be aided by the laser beam position dependences in Sec. V. In Sec. IV B, the types of stress and strain that give rise to the signals in Fig. 4 are examined using the results of Sec. III.

B. Analysis: stress and strain detection sensitivity

To determine the FM signal sensitivity to phonon stress and strain, an individual stress component will be separated out as described by Eqs. (10). Figure 5 shows the linear sums and differences of the S_2^{+45} and S_2^{-45} traces taken from Figs. 4(a) and 4(b). Figure 5(a) is proportional only to the time variation of the σ_{zx} stress or ϵ_{zx} strain. Figure 5(b) is proportional to a linear combination of diagonal stress σ_{ii} or strain ϵ_{ii} components. The S_2^0 signal from Fig. 4(b) is presented in Fig. 5(c) for comparison. Comparison of Figs. 5(b) and 5(c) shows that they are qualitatively similar, which is consistent with the idea that each is a linear sum of σ_{ii} [Eqs. 10(b) and 9(c)]. Before computing the sensitivity to stress and strain, a few initial comments about the varieties of stress and strain giving rise to the L and T signals shall be made, which will be used in phonon identification in later sections.

The largest features in the ϵ_{zx} trace in Fig. 5(a) are the T_1 and T_2 derivative shapes. Note that the T_1 and T_2 derivative shapes are missing from Fig. 5(b). Instead, the T_1 and T_2 signals in Fig. 5(b) each consist of broad, positive frequency swings. In other words, the derivative shape in the T_1 and T_2 signals results only from ϵ_{zx} shear strain. Also note that the T_1 and T_2 derivative shapes are about the same size in Fig. 5(a), but in Fig. 5(b) the T_1 positive peak is larger than the T_2 peak. Thus the T_1 and T_2 signals have similar ϵ_{zx} shear strain, but dissimilar sums of ϵ_{ii} axial strain components.

In contrast to the T signals in Fig. 5(a), the largest signals in Figs. 5(b) and 5(c) are the L features. Note that the L signals are largely missing from Fig. 5(a). Hence, the L signals result only from axial stress σ_{ii} or strain ϵ_{ii} components.

The sensitivity of the technique to an individual stress or strain component is computed as follows. With 1500

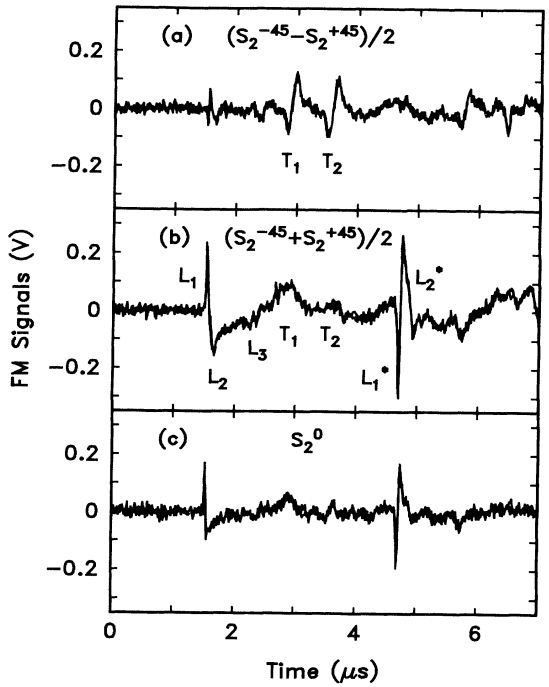

FIG. 5. Combinations of phonon time-of-flight signals for different probe-laser polarizations. Traces (a) and (b) are combinations of the S_2-phase signals shown in Fig. 4. (a) The difference of S_2-phase signals for probe-laser polarizations at $+45°$ and $-45°$ [i.e., the difference of S_2 traces in Figs. 4(a) and 4(b)]. (b) The sum of $+45°$ and $-45°$ polarization S_2 traces from Figs. 4(a) and 4(b). (c) The S_2-phase signal measured with horizontal (0°) probe polarization for comparison with the combinations in (a) and (b).

averages and a 20-MHz bandwidth, the S_2 signals have a noise level which is 5% of the peak of the S_2 spectrum, or about 38 mV in Fig. 4. The slope at the center of the S_2 spectra for Fig. 4 is found using the slope in Fig. 3(b) and the S_1 to S_2 signal spacing in Fig. 4 to be about 14 mV/MHz. [Computing the prefactor F/Γ in Eq. (7) gives about 10 mV/MHz, if one uses 0.75 V as a conservative guess for δ_p, and $\Gamma=250$ MHz. We will use $F/\Gamma=14$ mV/MHz below.] The noise level in the combination of signals $(S_2^{-45}-S_2^{+45})/2$ in Fig. 5(a) is $38/\sqrt{2}=27$ mV. Hence, a signal-to-noise ratio S/N=1 in $(S_2^{-45}-S_2^{+45})/2$ corresponds to an average frequency shift of the PSH spectrum by 27/14=2 MHz, which coincidentally is the jitter linewidth of the laser. Utilizing $F/\Gamma=14$ mV/MHz to convert the proportionality in Eqs. (9) and (10) to an equality, the σ_{zx} producing S/N=1 in Fig. 5(a) is $\sigma_{zx}=220$ N/m^2=0.002 atm. The corresponding shear strain is $\epsilon_{zx}=\sigma_{zx}/2C_{44}=4\times10^{-9}$.

One should keep in mind that the values computed above are averages over the probe volume, which the phonons may not uniformly irradiate. In general, crystalline elastic anistropy causes the phonon group velocity and the phase velocities to have different directions. A large solid angle of phase velocity is often channeled into a small solid angle of group velocities resulting in an en-

ergy flux enhancement in certain crystal directions. This phenomenon has been termed phonon focusing.[36] Energy focusing factors for special crystal directions have been computed by Maris,[36] which give values between 3 and 0.4 for NaF at low temperatures. Elastic wave energy is quadratic in the stress and strain. Hence for S/N=1 in Fig. 5(a), the corresponding shear stress and strain fields inside the probe volume may have peak magnitudes larger than 220 N/m^2 and 4×10^{-9} by a factor of $\sqrt{3}$.

These results may be compared and contrasted to the earlier phonon detection experiments of Lengfellner *et al.*[14] The acoustic echoes detected by observing the changes in transmission at the center of the spectral hole were not sensitive to the phase of the ultrasonic pulse. The sensitivity of our FMS approach is sufficient to exceed the strain sensitivity of the earlier work with an increased time resolution (from 5 μs to 50 ns), and allow for phase-sensitive detection of phonons up to 20 MHz. While this simple comparison has not precisely included the difference in detection bandwidth for the two experiments, it is clear that at least the phase sensitivity of the FMS approach is unique.

V. LASER POSITION DEPENDENCE AND PHONON IDENTIFICATION

A. Experimental results

To further investigate the origin of the various signals in Figs. 4 and 5, the pump and probe beam positions are varied. Figure 6 shows YAG spot position dependence with a 0.1-cm diameter YAG spot horizontally centered ($y=0$), but with different vertical positions (different z). The YAG spot z positions are indicated on the side of Fig. 6. The FM probe beam is vertically centered ($z=0$), and set near the middle of the crystal at $x=1.07$ cm. For the traces in Fig. 6, a single persistent spectral hole was burned and probed with +45° laser polarization. By examining Fig. 6, one observes that the L signals depend little on the YAG spot vertical position. By contrast, the derivative-shaped T signals show a strong dependence on the YAG spot position.

As the YAG spot moves through the probe-laser plane $z=0$, the derivative shaped portion of the T signals become narrower, disappear for $z=0$, and reappear with the opposite sign and broaden again. When the YAG spot is centered in the plane of the probe laser, the T signals that remain appear to be the positive frequency swings found in Fig. 5(b). In other words, the positive and negative parts of the σ_{zx} derivative-shaped T signals overlap in time and cancel when the lasers are vertically centered in the crystal. A possibility for the change in sign of the σ_{zx} derivative shape is that two different stress pulses containing σ_{zx} of opposite sign travel over different paths to the probe beam. With the YAG laser centered, these path lengths balance and the combined σ_{zx} stresses cancel. With the YAG beam vertically off center, the paths are not the same length and the σ_{zx} of one sign arrives before the σ_{zx} of the other sign. In other words, these paths involve some vertical (z) component of motion, so that one path becomes shorter and the other longer by vertical YAG displacement. To further investigate the different paths that the phonons follow, the probe beam is also displaced within the crystal.

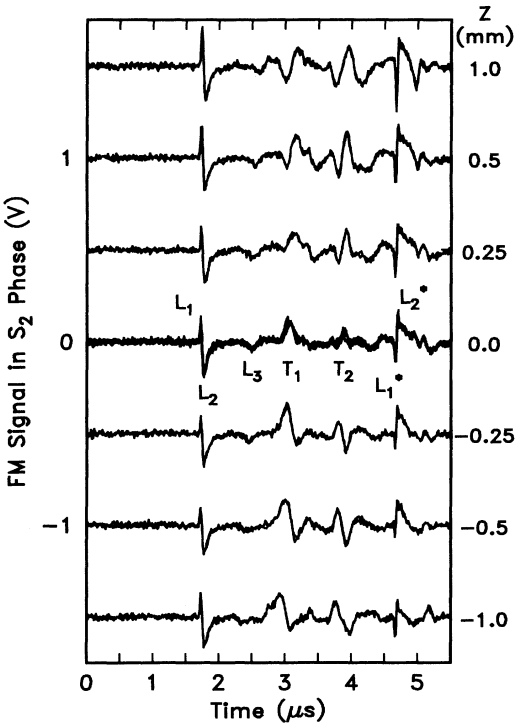

FIG. 6. Nd:YAG laser spot position dependence of the S_2-phase phonon time-of-flight signals. For each trace, the 0.1-cm-diam Nd:YAG laser spot is horizontally centered on the crystal end face ($y=0$) and set at a different vertical position (z), as indicated on the side of the figure. The probe-laser position is fixed in the middle of the crystal, and the probe polarization is set at +45° from horizontal. Each trace is an overlay of at least two traces (fives traces for $z=0$, three taken before, and two after the other traces), each of which is an average of over 1500 Nd:YAG laser shots.

Figure 7 shows the pulsed phonon signal dependence on the probe beam horizontal position. The YAG laser spot is centered on the crystal end face. The probe beam is vertically centered ($z=0$) and displaced horizontally in increments of about 0.15 cm. The probe beam x values are shown on the side of Fig. 7. For each probe-laser position, a new persistent spectral hole is burned and probed with +45° probe-laser polarization. Dashed lines are drawn in Fig. 7 to mark the movement of the various signals as the probe beam moves.

Considering the L signals for the moment, one sees that L_1 and L_2 arrive later and L_1^* and L_2^* arrive earlier as the probe laser moves away from the Cr. It is apparent that L_1 and L_2 are two parts of a single signal, and similarly for L_1^* and L_2^*. The L_1-L_2 arrival time is consistent with longitudinal acoustic (LA) phonons traveling in a [100] crystal direction at $(6.24\pm0.03)\times10^5$

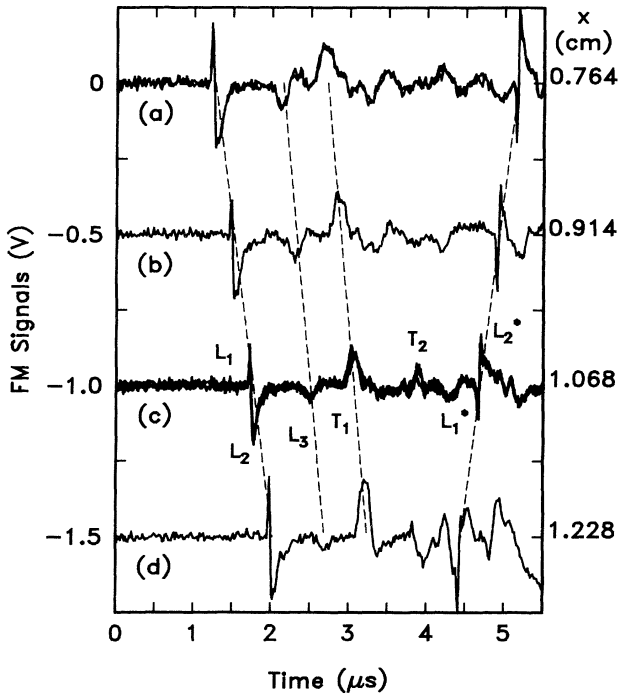

FIG. 7. Phonon time-of-flight signal dependence on probe-laser position. For each trace, the probe laser is positioned inside the crystal at a new distance from the Cr surface and a new persistent spectral hole is burned with +45° probe polarization. The probe distance from the Cr surface is indicated on the side of the figure. The phonon time-of-flight signals are measured in S_2 phase. The YAG laser firing time is at zero on the time axis. The dashed lines in this figure trace the movement of the phonon signals as the probe position changes.

cm/s, which is the highest acoustic velocity in NaF. As the probe laser moves away from the Cr, it moves closer to the other end of the crystal. The decreasing L_1^*-L_2^* arrival time is consistent with the return of the LA [100] phonons to the probe-laser volume after a reflection from the far crystal surface. In longer time traces (not shown here), as many as ten reflected LA [100] phonon pulses are observed, with the time interval between every other pulse corresponding to a LA [100] phonon round-trip time in the crystal. As observed in Fig. 7, the reflected L_1^*-L_2^* signal is opposite in sign to the L_1-L_2 signal. After each reflection, a sign change is observed, so that LA [100] phonons traveling in the $+x$ direction have the L_1-L_2 sign, and reflected LA phonons traveling in the $-x$ direction have the L_1^*-L_2^* sign. This 180° phase change is expected for an acoustic wave reflected at an interface of low acoustic impedance to high acoustic impedance, such as the NaF-He interface.[37,38]

The movement of two other signals can clearly be followed in Fig. 7. The L_3 and T_1 signals also arrive at later times as the probe laser moves away from the Cr surface, but more slowly than at a fixed multiple of the L_1-L_2 LA [100] arrival time. Data similarly taken with the YAG spot off center show that the ϵ_{zx} T_1 derivative shape (see Fig. 6) follows the movement of the ϵ_{ii} T_1 peak in Fig. 7. It is difficult to follow the movement of the T_2 signal, as the region after the T_1 signal becomes complicated for some probe-laser positions. A possible reason for this will be explored in Sec. V B.

The data in Fig. 7 are presented in a different way in Fig. 8 to aid further in signal identification. In Fig. 8, the time axis for each trace in Fig. 7 has been normalized to the L_1 pulse arrival time, which transforms the time axis to a relative velocity axis for [100] propagating phonons. In particular, [100] propagating transverse acoustic (TA) phonons, which travel at approximately $\frac{1}{2}$ the LA [100] speed, should produce a signal near 2 on the relative time axis in Fig. 8. Remarkably, an examination of Fig. 8 shows that there are no additional signals that line up, i.e., the TA [100] phonons appear to be missing. Signals that do not line up when the time axis is converted to a relative speed axis as in Fig. 8 must either (1) result from delayed emission from the surface, (2) do not travel in [100] crystal directions, or (3) do not travel ballistically (at constant speed). The present data cannot be used to rule out possibilities (1) or (3), but condition (2) is the most reasonable possibility consistent with the results of Figs. 6 and 7.

In Fig. 6, it was found that different paths are followed by the positive and negative parts of the ϵ_{zx} pulses in the T_1 and T_2 signals. Also, these paths involve some vertical component of motion, so that one path becomes

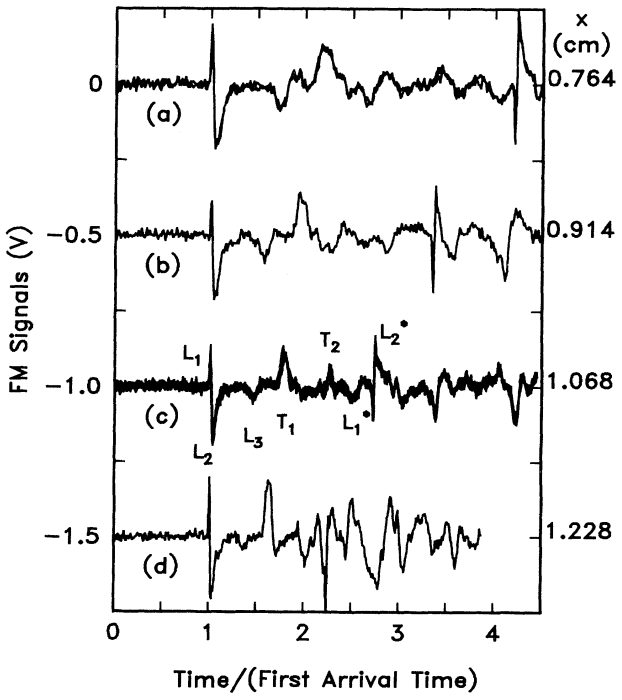

FIG. 8. Phonon time-of-flight signal dependence on probe-laser position with normalized time axis. The data in Fig. 7 are presented with the time axis for each trace divided by the L_1 signal arrival time.

shorter and the other longer by vertical YAG displacement. This is consistent with one possibility from Fig. 8 that the T_1 and T_2 signals are not from TA phonons propagating in nearly the [100] crystal direction. In order to have both a vertical component of motion and to reach the probe volume, these phonons must reflect off the upper and lower side walls of the crystal. One may then propose that the L_3, T_1, and T_2 signals all result from phonons propagating in directions widely different from the [100] crystal direction. In Sec. V B, an identification of the L_3, T_1, and T_2 signals as side-wall-reflected phonons is made.

B. Analysis: phonon identification

Three different concepts about phonon generation and propagation in crystals are used in this section to explain the various phonon stress-strain signals observed in NaF. The main results are reviewed below and then discussed in terms of the phonon hot spot at the surface, phonon focusing in crystals, and phonon mode conversion upon reflection. The features observed by measuring the stress and strain of pulsed phonons inside of a NaF crystal are summarized as follows. The LA [100] propagating phonons are the first phonons to arrive and consist of a compressional pulse followed by a dilational tail (L_1-L_2). TA [100] phonons are expected to arrive at nearly twice the LA [100] phonon arrival time, but are not observed by our choice of geometry and polarizations. Instead of observing the TA [100] phonons, many other phonon signals are observed (L_3, T_1, and T_2), and their behavior is consistent with side-wall-reflected phonons traveling in directions widely different from the [100] crystal direction. The ϵ_{zx} shear strain and ϵ_{ii} axial strain portions of the T_1 and T_2 signals have been separated, as in Fig. 5. The T_1 and T_2 derivative shapes result from ϵ_{zx} shear strains and are about the same in size [Fig. 5(a)]. The ϵ_{zx} strains reflected from the upper crystal face are opposite in sign to those reflected from the lower crystal face, and the difference in arrival times for an off-center YAG spot produces the positive and negative going derivative shape. The sum of axial ϵ_{ii} strain components for T_1 and T_2 appears to be compressional, and the T_1 peak is larger than that for T_2 [Fig. 5(b)]. The small L_3 negative frequency shift of the hole appears to involve a dilational sum of ϵ_{ii} axial strains.

In order to discuss phonon propagation within a crystal and mode conversion upon reflection, it is necessary to introduce the slowness and group-velocity surfaces. Figure 9 shows the slowness and group-velocity surfaces computed for NaF at 4 K in a (001) crystal plane. These have been computed using published formulas[39] and 4-K elastic constants.[40] The slowness vector is in the same direction as the phase velocity or **k**, but has a magnitude that is the reciprocal of the phase velocity. There are three such surfaces [Fig. 9(a)]. The outermost surface with circular cross section in the (001) plane is the pure shear or pure transverse (PT) surface, and has polarization normal to the (001) plane. The surface degenerate with the PT surface in ⟨100⟩ crystal directions is the quasitransverse (QT) surface, and has polarization in the plane, but not necessarily normal to the slowness or **k** direction. The innermost surface is the quasilongitudinal (QL) surface, with polarization in the plane and nearly parallel to **k**. A point on the surface specifies the direction of the slowness or the wave vector **k**. As shown in Fig. 9(a), the normal to the slowness surface specifies the direction of the corresponding group velocity $\mathbf{V}_g$. Note that the group velocity and phase velocity are not necessarily in the same direction. Most of the normals to the QT surface point in directions close to the ⟨110⟩ directions. In other words, large solid angles of **k** for QT phonons are channeled into small solid angles of group velocities near the ⟨110⟩ crystal directions. This channeling of the energy into a small solid angle is known as phonon focusing.[36] The concave shape of the QT surface produces the cusps in the group-velocity surface in Fig. 9(b), and these are a characteristic signature of phonon focusing.[26]

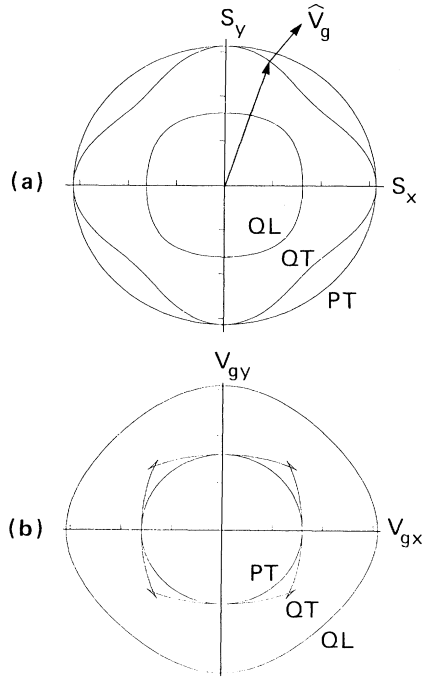

FIG. 9. Slowness and group-velocity surfaces for NaF at 4 K. (a) The acoustic wave slowness surfaces are shown in the (001) crystal plane. The fiducial marks in (a) are spaced 1×10^{-6} s/cm apart. The normal to a slowness surface gives the direction of the group velocity $\hat{\mathbf{V}}_g$. (b) The corresponding group-velocity surfaces are shown in the (001) plane. The fiducial marks in (b) are spaced 2×10^5 cm/s apart.

Inspection of the QL surface in Fig. 9(a) shows that there is some enhancement of the QL phonons not in the ⟨110⟩ directions, but rather in the ⟨100⟩ directions. Focusing factors expressing the amount of enhancement in high symmetry directions have been calculated.[36] Us-

ing 4-K elastic constants[40] to compute the enhancement factors for NaF, one finds that QL phonons are enhanced by a factor of 3.0 near the ⟨100⟩ directions, and that QT phonons are enhanced by a factor of 2.3 near the ⟨110⟩ crystal directions. Enhancement of the LA phonons in the ⟨100⟩ crystal directions is consistent with the strong LA [100] phonon signal labeled L_1-L_2. An explanation for the absence of [100] propagating TA phonon signals, which would have been measured by their ϵ_{zx} strains, is that the TA phonons are defocused from the [100] direction. However, TA phonons are focused in ⟨110⟩ directions, which gives rise to the variety of side-wall-reflected phonons, as explained below.

Phonon focusing considerations are consistent with the observation of a strong LA [100] phonon signal, no detectable TA [100] phonon, and most other signals appearing as side-wall reflections, if one takes into account mode conversion upon reflection. As is well known, reflection and transmission of a single acoustic mode at an interface generally involves acoustic mode conversion.[41,42] The L_3, T_1, and T_2 signals may then be explained as follows: LA phonons incident on the side walls (traveling in approximately the ⟨110⟩ crystal directions) are specularly reflected as LA phonons are partially converted to TA phonons. TA phonons incident on the side walls are reflected specularly as TA phonons and partially converted to LA phonons. The arrival times of the L_3 and T_2 signals are consistent with LA to LA and TA to TA side-wall-reflected phonons, respectively. Strong focusing of the TA phonons in ⟨110⟩ directions is responsible for the specularly reflected TA to TA T_2 signal appearing strongest when the probe-laser beam is centered horizontally in the x direction, as in Figs. 4 and 5. The complexity in the signals that arrive after passage of the T_1 signal in Figs. 7 and 8 can probably be attributed to a weaker distribution of phonon modes that are nonspecularly reflected upon mode conversion. The arrival time of the intermediate T_1 signal is consistent with both LA to TA conversion and TA to LA conversion upon reflection.

The sign and magnitude of the strains belonging to the observed TA phonons in T_1 and T_2 are also consistent with the side-wall reflection and mode-conversion identification. T_1 and T_2 signals both consist of ϵ_{zx} shear strains that travel to the probe volume after reflection from upper and lower side walls with opposite signs for ϵ_{zx} [Fig. 5(a)]. By examining Eq. (2), one sees that TA phonons that have ϵ_{zx} must be QT types of phonons, with $\mathbf{u}$ and $\mathbf{k}$ both containing components in the z-x plane. By performing the coordinate transformation $z \rightarrow -z$, one obtains $\epsilon_{-zx} = -\epsilon_{zx}$, i.e., by turning the crystal 180° about the x axis, the sign of the zx shear strain changes. This is consistent with the ϵ_{zx} shear component of the strain pulse reflected from the upper surface being opposite in sign to the pulse reflected from the lower surface. In Fig. 5(b), the larger sum of ϵ_{ii} for T_1, larger than for T_2, results from T_1 consisting of both mode-converted LA and TA phonons, whereas T_2 results only from TA to TA reflections without mode conversion.

The final result to be discussed is the appearance of the dilational tail following the compressional [100] propagating LA phonon packet. Heat pulses generated at surfaces with pulsed lasers have been known to produce a phonon "hot spot"[8] consisting of a broad spectrum of phonon excitations.[26,11] The experimental manifestation of the hot spot is a tail appearing after the initial phonon pulse as detected with a phase-insensitive bolometer, tunnel junction, or phonon-induced fluorescence. The explanation for the tail is that the elastic-scattering rate for phonons is exponential in the phonon frequency, which tends to trap high-frequency phonons near the surface. The high-frequency phonons decay anharmonically to lower-frequency phonons, which then escape from the surface region at a later time. With our phase-sensitive technique, we observe directly that the initial pulse is compressional in nature, and the hot-spot tail is dilational. This new observation within a single crystal at low temperatures is consistent with the hot-spot interpretation if thermal expansion and pressure relief are associated with the hot spot, as has been surmised from room-temperature experiments on metals.[43,44]

VI. CONCLUSION

Phase-sensitive optical detection of pulsed-laser-generated stress-strain waves inside of a solid has been demonstrated using frequency-modulation spectroscopy of a narrow persistent spectral hole in a NaF color-center zero-phonon line. Sensitivity of the FMS technique near the shot-noise limit and the spectral sharpness of PSH's produced a strain detectivity of 4×10^{-9} in a 20-MHz bandwidth. Focusing the probe beam diameter inside the NaF crystal to less than one-half the minimum acoustic wavelength expected for 20-MHz phonons in NaF allows the probe beam to follow the phase or sign of phonons up to the bandwidth limit of 20 MHz.

High sensitivity to strain led to a rich variety of observable phonon signals after pulsed laser generation. Identification of the various types of phonon packets was accomplished by selecting different rf phases of detection, by burning and probing PSH's with different laser polarizations, and by moving the phonon-generation and probe-laser beams relative to the crystal. The frequencies of differently oriented color centers were calculated to shift unequal amounts by a propagating stress-strain wave. By varying the probe-laser polarization, which varies the contribution by different color centers to the detected signal, it was possible to distinguish between propagating axial and shear strain components. The directions of propagation of the phonon packets were identified by displacing the phonon generation and probe-laser beams. A combined analysis of the traveling strain types, signs, and propagation directions led to an identification of the various phonon-packet polarizations.

Direct extensions to this work could include observations of the dilational or compressional nature of surface-generated ballistic phonon packets propagating in different crystal directions without side-wall reflection, phase change, and accompanying mode conversion.

Since PSH burning is found to occur in the defect absorption spectra of many different types of solids,[15] the phase-sensitive phonon-detection technique demonstrated here should also be applicable to the study of diffusive phonon propagation in glasses and polymers, as well as to ballistic phonon propagation in crystals.

ACKNOWLEDGMENTS

The authors wish to acknowledge helpful discussions and a critical reading of the manuscript by A. J. Sievers and the loan of the Nd:YAG laser from J. D. Swalen. This work was supported in part by the U.S. Office of Naval Research.

[1]See *Nonequilibrium Phonons in Nonmetallic Crystals,* Vol. 16 of *Modern Problems in Condensed Matter Sciences,* edited by W. Eisenmenger and A. A. Kaplyanskii (North-Holland, Amsterdam, 1986), and references therein.

[2]R. J. von Gutfeld and A. H. Nethercot, Jr., Phys. Rev. Lett. **12**, 641 (1964).

[3]R. J. von Gutfeld, in *Physical Acoustics,* edited by Warren P. Mason (Academic, New York, 1968), Vol. V, pp. 233–291.

[4]B. Taylor, H. J. Maris, and C. Elbaum, Phys. Rev. Lett. **23**, 416 (1969).

[5]B. Taylor, H. J. Maris, and C. Elbaum, Phys. Rev. B **3**, 1462 (1971).

[6]G. A. Northrop and J. P. Wolfe, Phys. Rev. Lett. **43**, 1424 (1979).

[7]J. P. Wolfe, Phys. Today **33** (12), 44 (1980).

[8]J. C. Hensel and R. C. Dynes, Phys. Rev. Lett. **39**, 969 (1977).

[9]M. Greenstein, M. A. Tamor, and J. P. Wolfe, Phys. Rev. B **26**, 5604 (1982).

[10]K. F. Renk and J. Diesenhofer, Phys. Rev. Lett. **26**, 764 (1971).

[11]K. F. Renk, in *Nonequilibrium Phonons in Nonmetallic Crystals* (Ref. 1), p. 277.

[12]R. S. Meltzer and R. M. Macfarlane, Phys. Rev. B **32**, 1248 (1985).

[13]D. Boye, W. Grill, J. E. Rives, and R. S. Meltzer, Phys. Rev. Lett. **61**, 1934 (1988).

[14]H. Lengfellner, T. R. Gosnell, R. W. Tkach, and A. J. Sievers, Appl. Phys. Lett. **43**, 437 (1983).

[15]See *Persistent Spectral Hole-Burning: Science and Applications,* Vol. 44 of *Topics in Current Physics,* edited by W. E. Moerner (Springer-Verlag, Berlin, 1988).

[16]A. L. Huston and W. E. Moerner, J. Opt. Soc. Am. B **1**, 349 (1984).

[17]W. E. Moerner and A. L. Huston, Appl. Phys. Lett. **48**, 1181 (1986).

[18]K. Beck, U. Bogner, and M. Maier, Solid State Commun. **69**, 73 (1989).

[19]Gary C. Bjorklund, Opt. Lett. **5**, 15 (1980).

[20]M. D. Levenson, R. M. Macfarlane, and R. M. Shelby, Phys. Rev. B **22**, 4915 (1980).

[21]R. T. Harley and R. M. Macfarlane, J. Phys. C **16**, 1507 (1983).

[22]R. M. Macfarlane, R. T. Harley, and R. M. Shelby, Radiat. Eff. **72**, 1 (1983).

[23]G. C. Bjorklund, M. D. Levenson, W. Lenth, and C. Ortiz, Appl. Phys. B **32**, 145 (1983).

[24]W. E. Moerner and M. D. Levenson, J. Opt. Soc. Am. B **2**, 915 (1985).

[25]C. Hoss, J. P. Wolfe, and H. Kinder, Phys. Rev. Lett. **64**, 1134 (1990).

[26]G. A. Northrop and J. P. Wolfe, in *Nonequilibrium Phonon Dynamics,* edited by W. E. Bron (Plenum, New York, 1985).

[27]D. A. Hutchins, Phys. Acoust. **18**, 21 (1988).

[28]Y. Kanemitsu, Y. Harada, Y. Tanaka, N. Nakano, H. Kuroda, and K. Yamanaka, Jpn. J. Appl. Phys. **28**, 234 (1989).

[29]B. A. Auld, *Acoustic Fields and Waves in Solids* (Wiley, New York, 1973), p. 169.

[30]M. J. P. Musgrave, *Crystal Acoustics* (Holden-Day, San Francisco, 1970), p. 83.

[31]Auld, Ref. 29, p. 13.

[32]Musgrave, Ref. 30, p. 20.

[33]A. A. Kaplyanskii, Opt. Spectrosc. **16**, 329 (1964).

[34]G. Baumann, Z. Phys. **203**, 464 (1967).

[35]Auld, Ref. 29, p. 61.

[36]H. J. Maris, in *Nonequilibrium Phonons in Nonmetallic Crystals* (Ref. 1), p. 51.

[37]D. A. Hutchins, Phys. Acoust. **18**, 95 (1988).

[38]Auld, Ref. 29, p. 130.

[39]Musgrave, Ref. 30, p. 110.

[40]J. T. Lewis, A. Lehoczky, and C. V. Briscoe, Phys. Rev. **161**, 877 (1967).

[41]N. Joel, Phys. Soc. Proc. A **78**, 38 (1961).

[42]Musgrave, Ref. 30, p. 138.

[43]D. A. Hutchins, Phys. Acoust. **18**, 67 (1988).

[44]F. A. McDonald, Appl. Phys. Lett. **56**, 230 (1990).